ROTARY ACTUATORS BASED ON PNEUMATICALLY-DRIVEN

ELASTOMERIC STRUCTURES

By

XIANGYU GONG

A thesis submitted to the

Graduate School – New Brunswick

Rutgers, the State University of New Jersey

In partial fulfillment of the requirements

For the degree of

Master of Science

Graduate Program in Mechanical and Aerospace Engineering

Written under the direction of

Professor Aaron Mazzeo

And approved by

_____

_____

_____

New Brunswick, New Jersey

October , 2015

ABSTRACT OF THE THESIS

Rotary Actuators Based on Pneumatically-Driven

Elastomeric Structures

by XIANGYU GONG

Thesis Director:

Dr. Aaron Mazzeo

This thesis describes a unique mechanism − a soft rotary actuator − based on peristaltic motion and large strain of inflatable elastomeric materials, which consists of an inflatable stator paired with a rotor. Timed inflation and deflation of the air-filled bladders in the stators enable controllable rotational speed of the rotor (~18 RPM). With two configurations (Type 1 and Type 2), this rotary actuator is capable of having either an internal rotor for winch- or join-like applications or an external rotor that can serve as a wheel. Fabrication of these actuators employs the use of 3D-printed molds and meso-scale soft lithography. Characterizations of these two types of actuators (speed, torque, and power), along with demonstrations, provide a baseline for potential applications in locomotion and transportation of payloads. A squishy, four-wheeled vehicle enabled by Type 2 actuators travels at a speed of 3.7 cm/s, negotiates irregular terrain, and endures mechanical impact from a drop 7 times its height. This class of rotary actuators extends the potential functionality of soft robotic systems by providing torque without requiring the bending or twisting of tubing that provides pneumatic power.

ACKNOWLEDGEMENTS

Firstly, I would like to express my sincere gratitude to my advisor **Professor Mazzeo**, without whom I would not have come this far. He has taught me what the most valuable qualities are as a good researcher. His passion, persistence and immense knowledge motivated me to go even further and continue exploring the unknown in my future PhD study.

Besides my advisor, I would like to thank all my lab mates for the time we spent together in the group. My collaborations with the co-authors on this work – **Ke Yang**, **Jingjin Xie**, **Yanjun Wang**, **Parth Kulkarni**, and **Alexander Hobbs**, have been very creative, productive and fun! Without you, I would not have been able to finish this work.

Last but not the least, I would like to thank **my parents** for supporting me unconditionally and giving me the courage when I could not have made it. They inspire me to be a better person everyday.

Table of Contents

1. Introduction

Rotation plays a significant role in machines. Conventional robots often depend heavily on joints and torque-providing motors, but recent advances in pneumatic, elastomeric actuators are not capable of delivering torque through pure rotation. Pneumatic channels/networks based on elastomeric materials of differing geometries have gained wide applications. The pneumatic, artificial McKibben muscles, for example, developed in 1950's and 1960's, contract when their volume increases due to pressurization, which usually provides a linear motion[1].

In the 1990's, Suzumori et al. used flexible microactuators (FMAs) to create multi-fingered robotic manipulators[2]. They also developed soft-bodied swimming robots, inspired by the manta ray[3]. Both of these designs relied on cooperative motions of their pneumatically-driven components, in order to complete complicated tasks, such as manipulating an object, screwing a bolt, or swimming underwater. Pneumatic networks (PneuNets) designed by the Whitesides Group consisted of a series of inflatable chambers embedded in elastomers[4]. With these inflatable structures, they demonstrated complex motion at varying speeds. Relying on the simple motion of bending, soft grippers manipulated fragile objects with pressurized fingers. Multigait soft robots crawled and undulated by changing their gaits[5]. Further demonstrations have also included camouflage[6], resistance to puncture and impact[7], elastomeric origami-like devices[8], soft robots powered by explosions[9], fast PneuNets (fPNs)[10], and an untethered soft robot resilient to adverse environments[11]. However, these soft robots introduced above have generally relied on two fundamental modes of motion: bending and extension.

Researchers have also made rolling, belt-like robots[12,13] and a spherical rolling robot[14], which did not employ soft wheel-and-axle structures. Their structures (circular belts and spheres) enabled rotation and might be capable of higher rotational speeds in the future. Nonetheless, vehicles that rotate completely upon themselves might have difficulty in transporting payloads and handling pneumatic tubing.

We explore a unique configuration of inflatable stators paired with rotors. The design presented in this paper provides another mode: rotary motion, which is independent of bending or extension. This paper introduces two types of designs for the actuators integrated with multiple methods of fabrication and different materials. To demonstrate the application for these actuators, we built a winch equipped with rotary actuators, which is capable of applying torque to lift weights. For this type of actuator (Type 1), the stator with air-filled bladders surrounds an internal rotor. Another type of actuator (Type 2) has the stator inside its rotor, and the assembly functions as a wheel. Using the latter design with the stator inside the rotor, this work highlights the capability of fabricating physically compliant vehicles with soft wheels, which are capable of withstanding mechanical impact and maneuvering on land and in water.

2. Background

Current pneumatically-driven soft robots, such as starfish-like grippers[4,15], octopus arms[16–18], multigait locomotors[5], robotic tentacles[19], and manta rays[3] can mimic the motion and behavior of many kinds of soft animals. Nevertheless, in nature, many creatures consist of rigid structures with bones coupled to soft tissues, such as muscle, cartilage, and skin. In the case of limbs, these composite structures are capable of moving relative to each other, in part, because of their interconnecting joints. The ability to create joints that can rotate with multiple degrees of freedom remains an open challenge for soft robots. From the perspective of biologically inspired (bio-inspired) design, the rotary actuators described in this work are a step toward rotating, joint-like structures that might provide torque in future limbed robots with soft, synthetic components.

Furthermore, while many soft robots have their basis in bio-inspired design or evolution[18,20,21], wheels on axles – distinct from rolling mechanisms employed by animals, such as, armadillos[22], pangolins, wheel spiders and pebble toads – for soft machines are a notable exception[33,34], as these fully rotating components do not exist in nature at the mesoscale. Future limbed or wheeled robots with elastomeric components might find uses in search and rescue missions in extreme environments or over various terrains. With the low sensitivity of elastomers to electromagnetic radiation, wheeled robots or rovers made of elastomers might also facilitate travel in space or manipulation of objects during magnetic resonance imaging (MRI). Lacking sharp or metal components, soft rotary actuators may also serve as safe motors and be compatible with future human-friendly robots or vehicles.

Since the work of Karl Sims in the 1990's, there have been continual efforts to use genetic or evolutionary algorithms to explain and simulate efficient modes of motion in both soft and hard bio-inspired virtual creatures[23,24]. The competitively advantageous modes generated in simulation for soft creatures appear to resemble walking, crawling, and jumping[25]. Just as wheel-and-axle assemblies are absent from nature[34], soft wheels are absent in simulated results obtained through evolutionary algorithms, which adds to the uniqueness of the development of future soft rotating machines.

3. Experimental Design

3.1. Peristaltic Motion as a Mechanism for Providing Torque

Peristaltic motion is common in nature. Peristalsis generated by the circular muscle of human esophagus helps push a bolus of food toward the stomach[26]. People have applied peristaltic actuation into polymer-gel-based actuators that transport objects via oscillating reactions[27]. Researchers have also fabricated micropumps for drug delivery using peristaltic mechanics[28]. A variety of limbless crawlers, such as earthworms, snails and snakes, use peristaltic mechanics and have inspired multiple worm-like robots[29,30].

The inspiration of our design comes from the combination of peristaltic motion with the standard layout of a rotary motor consisting of a rotor and a stator. The stator is a circular, elastomeric structure with embedded, hollow bladders. Each bladder has an inlet that provides pressurized air. We divide or distribute the flow of pressurized air into multiple subgroups of bladders with each subgroup being inflated and deflated sequentially. The sequential inflations and deflations generate a peristaltic wave surrounding the stator. The peristaltic wave, offset some radial distance from the rotational center of the rotor, exerts a set of circumferential forces to provide torque on the rotor.

This work demonstrates two configurations of rotary actuators that enable the conversion of peristaltic motion to torque. In the first configuration, which we name Type 1, the stator surrounds the rotor. In the second configuration named Type 2, the stator sits inside the rotor. **Figure 1A** shows one complete cycle of sequential inflation of four subgroups of bladders on stators without rotors for both types of configurations. These
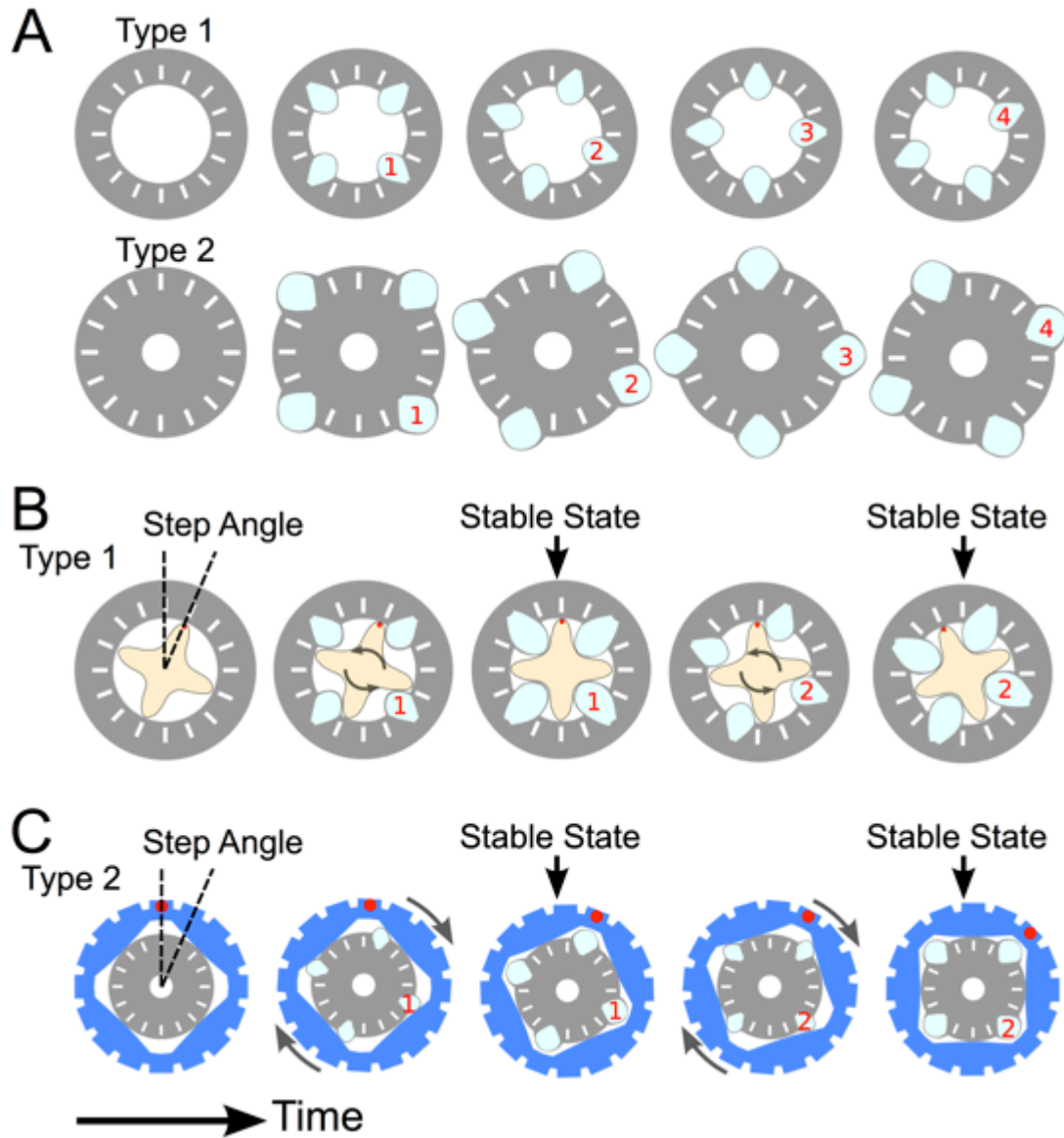
Figure 1. Basic configurations and sequential presentation of subgroups of embedded bladders for two types of soft rotary actuators. (A) Subgroups of bladders inflate around fixed stators in peristaltic fashion (1→2→3→4→1…). (B) An actuator with an internal rotor (Type 1) showing a step angle of 22.5°, along with rotation between stable states. (C) An actuator with an external rotor (Type 2) also showing a step angle of 22.5° and rotation between stable states.

two configurations lend themselves to unique sets of applications as shown through a prototype of a winch (Type 1) and squishy wheels (Type 2).

Type 1: As shown in **Figure 1B**, Type 1 consists of a stator and a cross-shaped internal rotor. Each time one subgroup of the air-filled bladders receives pneumatic pressure, the four growing bladders in the stator exert force/toque on the rotor to make it turn. The rotation stops when the bladders make contact with the internal corners of the rotor. This stop is a stable state. To move from this stable state, we exhaust the inflated subgroup and inflate an adjacent subgroup of bladders to transition the rotary actuator through another metastable step. The repeated sequence of inflation and deflation generates the staggered turning of the rotor. With increases in the frequency of sequential actuations, smoothness and continuous nature of the rotary motion also increase.

Type 2: As shown in **Figure 1C**, Type II has an external rotor. Instead of inflating toward the center of the stator as in Type I, the peristaltic wave travels along the outer surface of the stator with the applied sequence of inflation and deflation. Similarly, the groups of bladders exert forces on inner surfaces of the rotor surrounding the stator. While the bladders are inflating, the rotor turns until a group of bladders reaches a stable state. An adjacent group then inflates, and the rotor continues its rotation.

Step Angle: Like a conventional stepper motor driven by a series of pulsed signals, the inflation of each group of bladders drives the rotor of the soft rotary actuator to turn by a fixed angle, which we call a step angle. According to this principle of design, the rotor turns in discrete increments from subgroup of embedded bladders to subgroup of embedded bladders. Thus, the number of equally spaced bladders in the stator determines the step angle of the rotary actuator. In this paper, there are 16 bladders in the stators.

Thus, in each step (from one subgroup to the next subgroup), the rotor turns by 22.5° (360°/16).

3.2. Meso-scale Soft Lithography to Fabricate the Actuators

Using computer-based, geometric models created in SolidWorks (Dassault), a three-dimensional (3-D) printer (FlashForge Creator) produced Type 1 rotors and molds for elastomeric components. The Supporting Information (**Figure S1**) discusses more details concerning fabrication. In this paper, we made stators of a silicone-based rubber Ecoflex 00-50 (Smooth-On Inc.) by bonding the cured top layer to the partially cured bottom layer without applying an intermediate layer of adhesive as shown in **Figure S1A**. With these two layers, a stator contains closed rectangular bladders (length: 0.5 cm, width 0.15 cm, depth: 0.5 cm) inside of it.

We also present methods for fabricating the two types of rotors (Type 1: 3.65-cm diameter, Type 2: 9.2-cm diameter). We fabricated the hard internal rotor (Type I) from thermoplastic acrylonitrile butadiene styrene (ABS) directly through the 3-D printer using computer-aid design (**Figure S1B**). On the other hand, we bonded three structured layers of molded elastomers to make external rotors (Type II) (**Figure S1C**). A 3-D printer produced the molds for each layer.

There is friction between the stator and the rotor. In order to reduce the friction and smoothe the rotation, we applied lubricant between the sliding interfaces of the rotor and stator. After qualitative experiments with different lubricants, including dish soap, water, silicone oil, and Super Lube grease (Synco Chemical Corp.), we concluded that Super Lube grease provided the smoothest rotation of these options. Super Lube grease is a

nontoxic synthetic lubricant with PTFE, and it does not drip or dry out easily. Moreover, it does not react with or significantly alter the texture of the elastomers.

3.3. Analysis of Strain with Pressurization of the Stators

A sufficient inflation of the bladders without damage is a prerequisite for enabling a continual rotation of the rotors. To understand how the pressurized air acted on the deformation of bladders, we estimated the strains on a stator during inflation with finite-element methods (FEMs) (**Figure S2A, C**). With uniaxial tensile test data for Ecoflex 00-50, we fitted the stress-strain curve to a 3rd-ordered Yeoh model of hyperelasticity (**Figure S3**) in a similar fashion to the work completed by Mosadegh, et al.[10] Given a specified static internal pressure, the simulations showed the volumes of a subgroup of bladders and their corresponding maximum principal strains when pressurized. The maximum principal strain (~200%) did not exceed maximum strain at break of the Ecoflex 00-50 (980%) provided by the manufacturer, which means the bladders might not yield at the applied pressure (varying from 0 to 62.1 kPa).

We then validated the FEM simulations qualitatively by comparing the deformation of stators caused by internal pressure with experimentally acquired images (**Figure S2 B, D**). Because a stator consists of two separate layers that were bonded together, these experiments also proved the applied internal pressure that sufficiently enabled the rotation would not cause the delamination between the bonded parts. More details regarding the results of the simulations and the experimental images are in the Supporting Information.

3.4. Programmable Pneumatic System and Speed Control

We built a programmable pneumatic system (**Figure S4**) installed with 3-port, 2-position solenoid valves (SMC Inc.) to control and direct pressurized air to the inflatable bladders in the rotary actuators. A Type 700 high-flow pressure regulator (ControlAir Inc.) regulated the pressure for the inflation, with a pressure gauge (ASHCROFT Inc.) monitoring the pressure. To control the timing of the solenoids accurately, we used an FPGA-based NI cRIO-9076 with two 8-channel, 1 μs high-speed digital output modules NI 9474 from National Instruments. The software is similar and the LabVIEW Virtual Instruments are nearly identical to the pneumatic system employed for multi-gait, reconfigurable, and camouflaging robots[5,6].

Once assembled, inflation of the bladders in the stator caused the rotor to turn. To reduce the fatigue and excessively large deformation caused by higher alternate pressure loads on the bladders, and to avoid yielding of the material, we always inflated the bladders to a constant volume – the minimum inflation that makes the rotor turn consistently. With the pneumatic system equipped with the specified solenoid valves, pressure regulator, and tubing, we could change the flow rate of the pressurized air filling in the bladders by regulating the pressure with the regulator. Higher flow rate of air induced higher inflation rate of the bladders, thus, a shorter time was needed to inflate each subgroup of bladders to the minimum volume required. While this minimum volume had an associated static internal pressure, the use of a standard regulator meant that we would typically set a pressure on the regulator that might otherwise cause a larger static deformation. In this way, the bladders inflated quickly to the minimum volume

when a solenoid then cut off the airflow before the actual internal pressure in the bladders reached the pressure set on the regulator.

In addition to controlling the rate of inflation, we needed to allow a period of time to exhaust the air from a group of bladders before inflating an adjacent group. Thus, the rotational speed of the actuators relied on both times of inflation and deflation for each group of bladders. **Figure 2A** depicts the staggered inflation and deflation of four subgroups of bladders embedded in a stator. The blue solid lines represent the command signals for the opening and closing of the valves. Each valve associated with a group of bladders opened and subsequently closed to control the air flowing into these corresponding bladders. Here, the period between opening and closing of the valve was the inflation time $t_{\text{inflation}}$, which was also the time needed to inflate a group of bladders to the minimum volume. The red dotted lines indicate the change in the internal pressure/volume within the bladders. As the internal pressure approached the pressure corresponding to the minimum volume that could enable a consistent rotation of the rotor, we halted the inflation by switching the position on the valves to cut the pressurized airflow and exhaust the air in the bladders to the atmosphere. Unlike inflation times, which are dependent on the pressure set on the regulator, the deflation times remain consistent for a given volume of the inflated bladders. To get the time of deflation $t_{\text{deflation}}$, we used a high-speed camera (120 frames/second) to record the deflation of each group (**Figure S5**, **Movie S1**). In this way, we found the average deflation times of Type 1 and Type 2 actuators were approximately 130 msec and 190 msec, respectively.
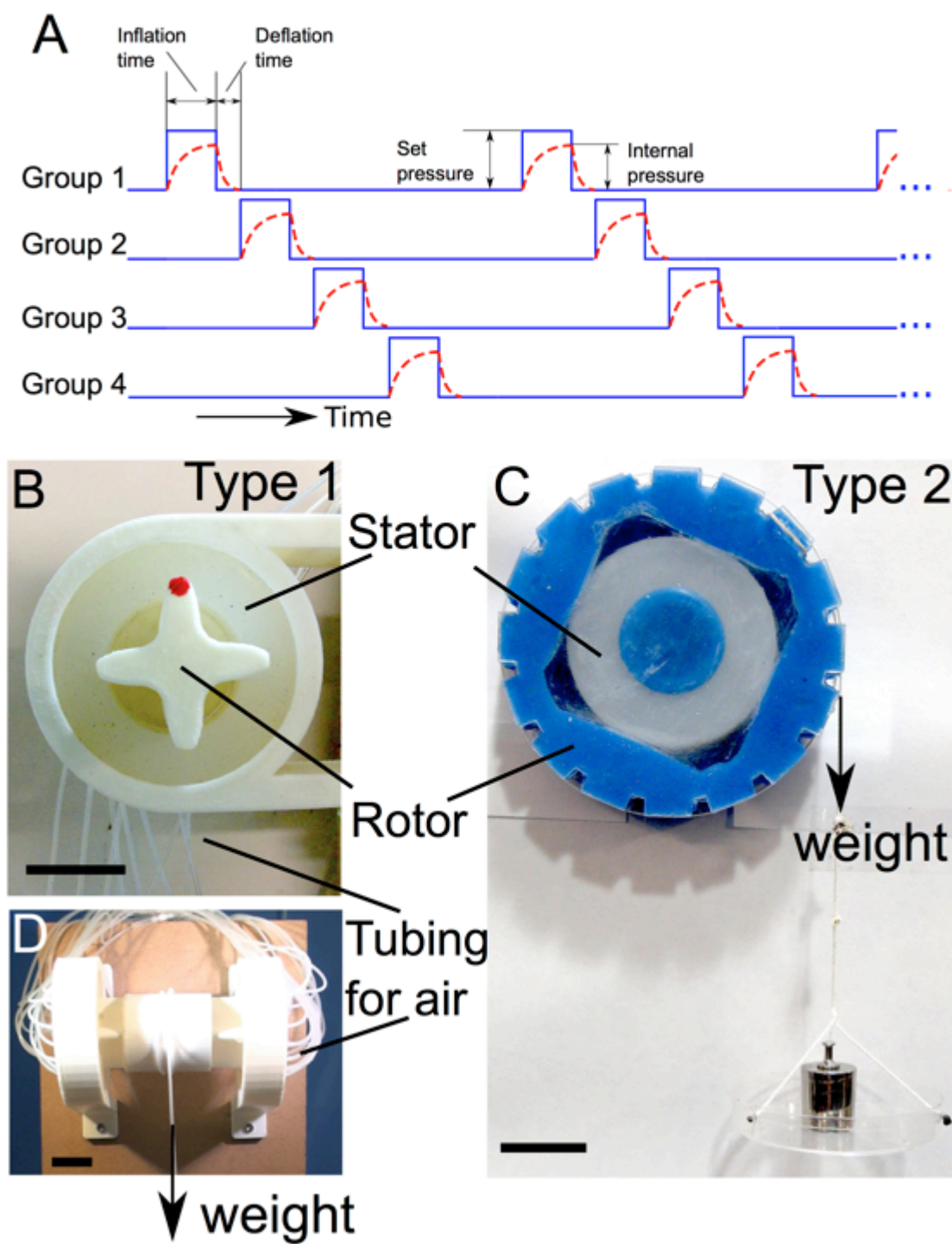
A Inflation time Deflation time Set pressure Internal pressure Group 1 Group 2 Group 3 Group 4 Time

B Type 1 Stator Rotor Tubing for air

C Type 2 weight

D weight

Figure 2. Controllable setups used for characterization. (A) The sequential inflation and deflation of groups of bladders. Four solenoid valves opened and closed to deliver pressure to four groups of bladders. (B) Experimental setup for characterizing "set pressure – rotational speed" for Type 1 actuators. (C) A Type 2 actuator attached with a light-weighted string for external load. We used this setup to characterize this actuator. (D) Experimental setup for easily profiling the relationships between rotational speed of Type 2 actuator and the external torque acting on it. The scale bar is 2 cm.

With an approach similar to that of controlling a DC motor by changing the applied voltage, we manipulated the speed of the rotary actuator by varying the pressure set on the regulator. With a specific inflation time corresponding to a specific set pressure, we calculated the rotational speed with the following formula:

$$\text{Rotational Speed (RPM)} = \frac{(60 \text{ msec/min})(1000 \text{ msec/min})}{(16 \text{ group/rotation})(t_{\text{inflation}} + t_{\text{deflation}})} \tag{1}$$

The units of $t_{\text{inflation}}$ and $t_{\text{deflation}}$ are milliseconds (msec).

As mentioned previously, a higher set pressure caused a shorter inflation time. Therefore, characterizing this relationship was necessary, in terms of controlling the rotational speed of an actuator. **Figure 2B-C** represent the Type 1 and Type 2 actuators connected to the pneumatic system, respectively. We could attach an external load to the light-weight string on the Type 2 actuator. To profile the "set pressure – inflation time" relationship, we first specified an inflation time for the solenoids (i.e., command signals shown in **Figure 2A**), which could be easily set on the cRIO through a computer. Then, starting from a very low pressure on the regulator, we gradually increased the pressure until the bladders reached the minimum volume to enable the rotor to turn in one complete cycle (i.e., at least 16 steps). By varying the inflation times, we experimentally profiled that relationship of the inflation time and set pressures on the regulator. After profiling this "set pressure – inflation time" relationship, we mapped the characterization of "rotational speed – set pressure" by simply converting the inflation times to rotational speeds with **Equation 1** and previously measured deflation times. When performing this characterization, we did not add any external load on either type of actuators. Results and

Discussion includes the characteristic curves of "set pressure – inflation time" and "rotational speed – set pressure".

3.5. Characterization of Torque and Rotational Speed

People have characterized the relationship between external torque and rotational speed for motors. Similarly, in addition to our ability to control the rotational speed by manipulating the air pressure, we were also interested in how the rotational speed changed with an external load acting on the actuator at a fixed pressure on the regulator, in terms of applications of these rotary actuators in the real world. To examine the relationships between torque and the rotational speeds of both types of actuators, we kept using the basic setup for the Type 2 actuator shown in **Figure 2C**, by attaching external loads on the string. On the other hand, we built a symmetric experimental setup for the Type 1 actuator (**Figure 2D**), because we found it difficult to directly attach external loads to a single Type 1 rotor. The new setup consisted of two 3-D printed brackets, each fixing a stator inside. A cylindrical shaft bridged two Type 1 rotors on each of its ends, and a string was attached to the shaft. Detailed designs of the brackets and the shaft are in the Supporting Information (**Figure S6**). We then inserted the shaft with rotor-shaped ends into the stators. This "winch-like" setup allowed us to add up the weight easily and keep the rotors balanced and stable inside the stators when profiling the "torque – rotational speed" curve. By using this setup to perform the experiments, we had to divide the weight by 2 to get the external torque acting on one actuator.

For both actuators, we set a pressure of 68.9 kPa (around 10 psi) on the regulator and started pressurizing to make these actuators turn without any external loads. While adding up the external loads on the actuators, we expected more inflation time to

overcome the increased pressure force and friction between the rotor and stator caused by the increased load. Thus, increasing external torque acting on the actuators would lower the overall rotational speed due to longer inflation time needed.

In addition to the capability of transporting payloads as already shown during the characterization, we also demonstrated how the soft rotary actuators could be integrated with others' work (i.e., a soft gripper imbedded with PneuNet)[4]. A winch equipped with a soft gripper going up and down was able to manipulate/transport an object. (**Figure S7, Movie S2**)

4. Results and Discussion

4.1. Characteristics of Soft Rotary Actuators

To better understand the capabilities (i.e., rotational speeds and load capacity) of the actuators, we explored the actuators by characterizing them in similar fashion to characterizing DC motors. **Figure 3A** profiles the set pressures on the regulator corresponding to the desired inflation times for each subgroup of bladders with no external load on the rotors. **Figure 3B** shows the relationships between the rotational speed and the set pressures from the data shown in **Figure 3A**, the previously measured deflation times, and **Equation 1**. In general, increasing the set pressure on the regulator lead to a higher rotational speed, because the inflation time decreased due to increased flow rate. According to the curves, Type 1 achieves higher rotational speed than Type 2 with the same set pressures. The Type 1 rotor weighed less than the Type 2 actuators and qualitatively had less friction with its stator than the Type 2 actuators. The higher speed of Type 1 actuators than those of Type 2 is also because the bladders are acting on the
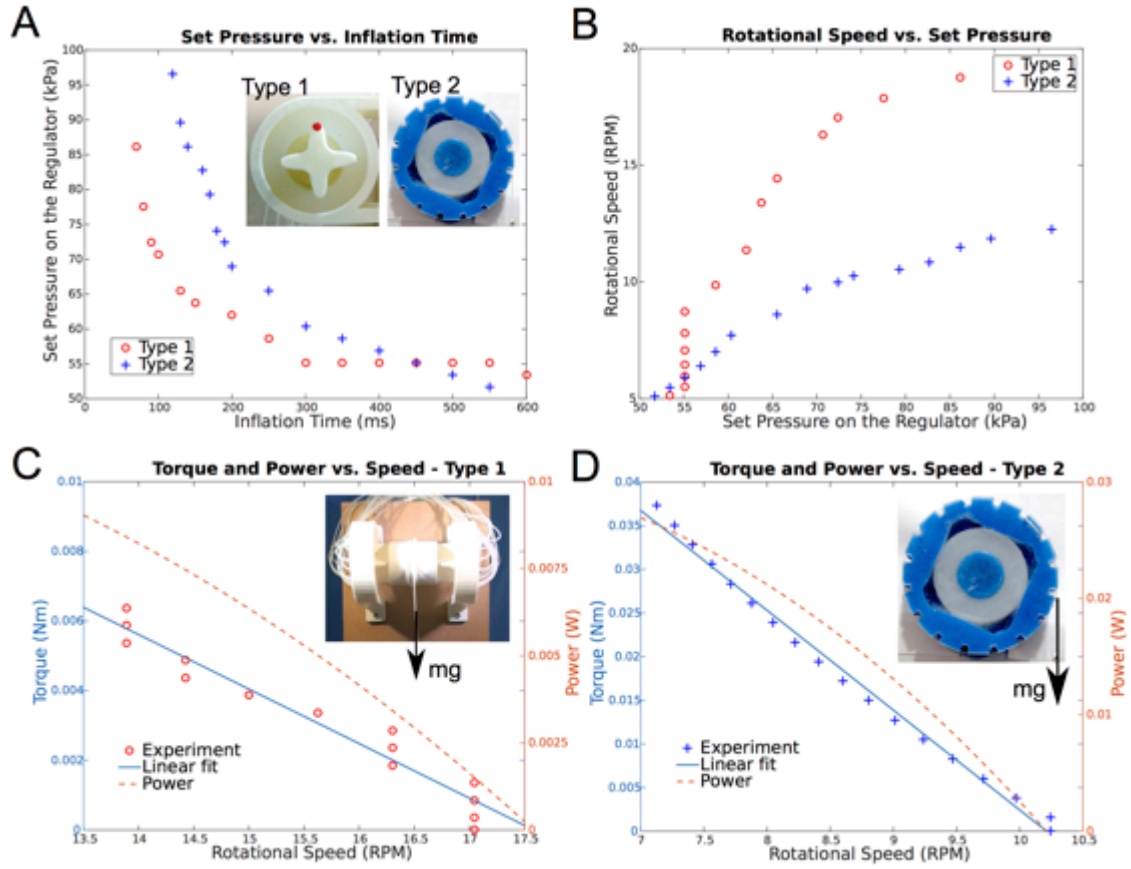
Figure 3. Characteristics of soft rotary actuators. (A) Measured relationships between set pressure on the regulator and inflation time for both types of actuators without any external load. (B) Calculated rotational speed as a function of set pressures for both types of actuators based on the measurements of (A). (C) Torque-speed characteristics of actuator Type 1 and the estimated power based on its linearized characteristics. (D) Torque-speed characteristic of actuator Type 2 and the estimated power based on its linearized characteristics.

rotors at a distance closer to the axis of rotation than in the Type 2 actuators. The bladders in both types inflate by approximately the same amount at the same rate, and as this action moves closer to the axis of rotation, the speed of rotation increase. There was also a remarkable change in the speed for the Type 1 actuator at around 55.2 kPa (8 psi) caused by the snap-through behavior of the inflatable elastomers[31,32].

Figure 3C-D characterized the rotational speeds of the two types of actuators, respectively, as a function of the torque at a specified pressure set on the regulator. Given the diameters of rotating units of the setups (the shaft of the winch: 4.05 cm; rotor of Type 2 actuator: 9.2 cm), we calculated the torque based on the external loads we added on them. At a fixed pressure of 68.95 kPa (10 psi), starting with no load, the winch for Type 1 rotated at the speed of 17 RPM approximately, and the Type 2 had the rotational speed of around 10.2 RPM. Here, we noted that the speed of Type 2 actuator matched the characteristics of "set pressure – rotational speed" (**Figure 3B**) well at a set pressure of 70 kPa (10.2 psi). However, the speed of the winch was higher than that of a single Type 1 shown in **Figure 3B**, which might be due to increased power of doubled actuators.

Generally, the rotational speeds of the actuators dropped when the external loads went up, until the torque reached 0.0065 Nm for Type 1, and 0.0375 Nm for Type 2. At that point, the actuators were no longer able to bear the external torque or turn continually, with the rotors sliding back inside the stators. Using linear regression, we approximated the relationships between rotational speed and external torque to a linear model, based on the experimental data. In this way, we could also estimate the power of the actuators as a function of the speed of rotation. According to the modeled "power – rotational speed" curves (orange dotted-lines) in **Figure 3C-D**, the maximum powers that the actuators

could achieve were 0.0084 W and 0.026 W, when the rotational speeds were at a minimum. The overall power of the Type 1 actuator was lower than that of Type 2, but the Type 1 actuator could achieve a higher rotational speed.

4.2. A Squishy, Wheeled Vehicle

To demonstrate the application of the rotary actuators powered by the pneumatic system, we built prototypes of squishy vehicles equipped with the actuators working as wheels with a diameter of 9.2 cm. Combining multiple controllable motions, a two-wheeled vehicle demonstrated the capability of navigating around an obstacle at a high speed (4.9 cm/s) when the pressure (set on the regulator) was 86.2 kPa (12.5 psi). (**Figure S8, Movie S3**)

We also extended the two-wheeled device to a rover-like vehicle with four wheels (**Figure 4A-B**). A structure made of Ecoflex 00-50 served as a chassis to connect two two-wheeled modules. In this paper, we did not address the issue of making the four-wheeled vehicle turn, which means it only moved in a straight line.

At the same set pressure of 86.2 kPa (12.5 psi) used to drive the two-wheeled vehicle, we needed longer inflation time (300 msec) to compensate for the extra loading associated with an increase in the total weight (1.23 kg) and friction between stators and rotors. The rotational speed of each wheel was 7.7 RPM, and therefore, the speed of the vehicle was 3.7 cm/sec (**Figure 4C-E, Movie S4**).
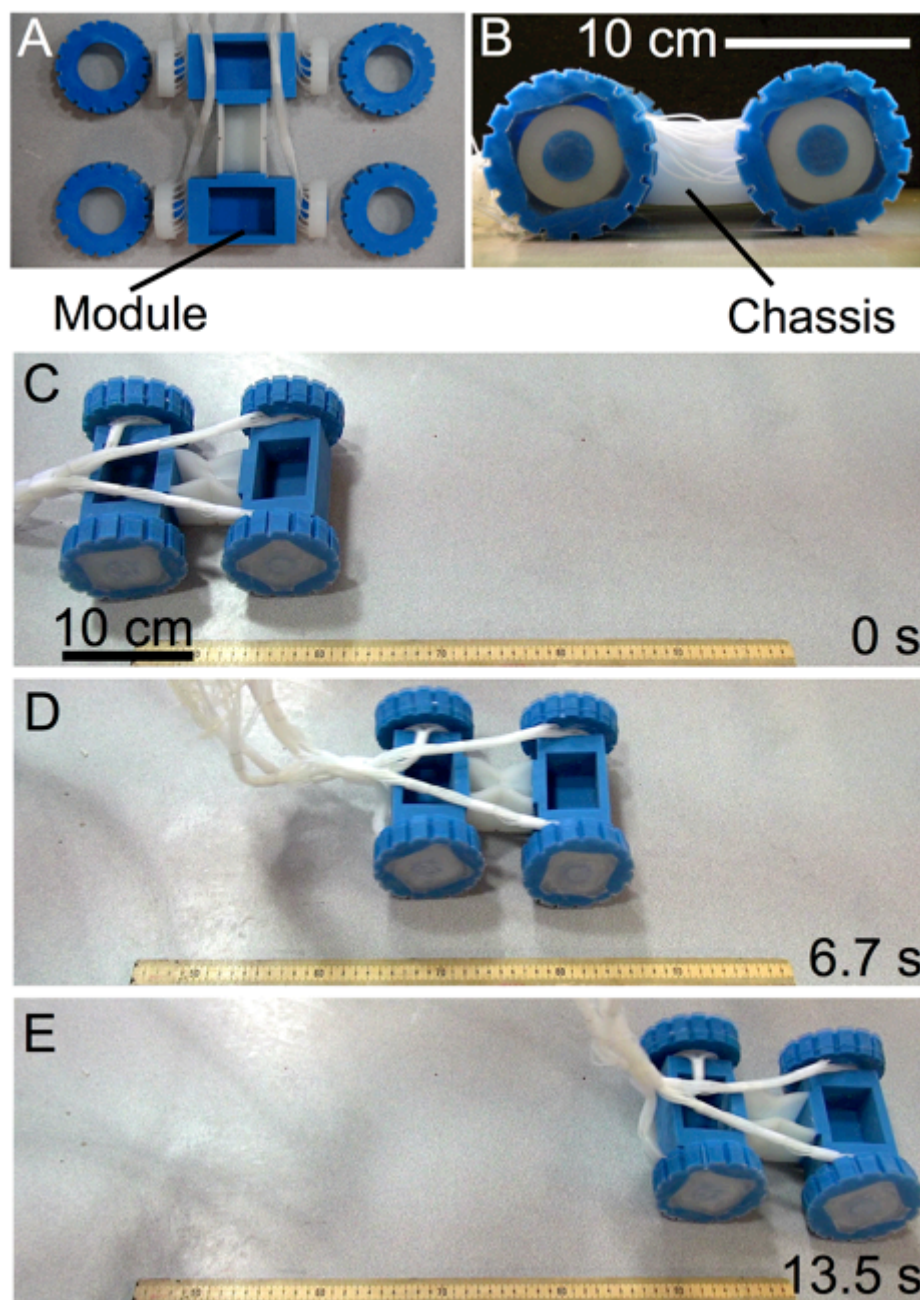
Figure 4. A squishy, four-wheeled vehicle. (A-B) Assembly of the four-wheeled vehicle.

(C-E) The vehicle is traveling on a flat surface without any obstacles, at a speed of 3.7

cm/s. (**Movie S4**)

This four-wheeled vehicle demonstrates several potential advantages when it comes to navigation of new/irregular surroundings or potential missions of rescue often involved with varied terrains. First, there were not any rigid components in the entire vehicle. Also, the oversized, elastomeric wheels could absorb mechanical impacts. Thus, this design would be able to withstand higher impact than one composed of rigid members[7]. A drop test from a height (0.72 m) of 8 times the vehicle's height did not cause any damage on the body or the actuators (**Figure 5, Movie S5**). After bouncing once and then landing on the ground safely, the vehicle continued to move forward.

Secondly, navigation over difficult terrain with a naturally compliant set of wheels and suspension has the potential to eliminate some of the complexity associated with rigid members and multi-component suspensions, which might require actuated lifting of wheels over obstacles. In **Figure 6** (and **Movie S6**), the squishy vehicle negotiated a rocky terrain with a puddle. As shown in **Figure 6B**, the chassis made of Ecoflex 00-50 bent to comply with the rugged landscape. From the puddle back to the higher area (**Figure 6C**), increased gravitational potential energy required lower rotational speed (i.e., a longer inflation time), or a higher pressure set on the regulator.

Additionally, the vehicle equipped with the actuators worked not only in a dry environment but also under water (**Figure S9, Movie S7**). The current design does not expose any metal components that might corrode to water and might inspire future low-cost amphibious vehicles.
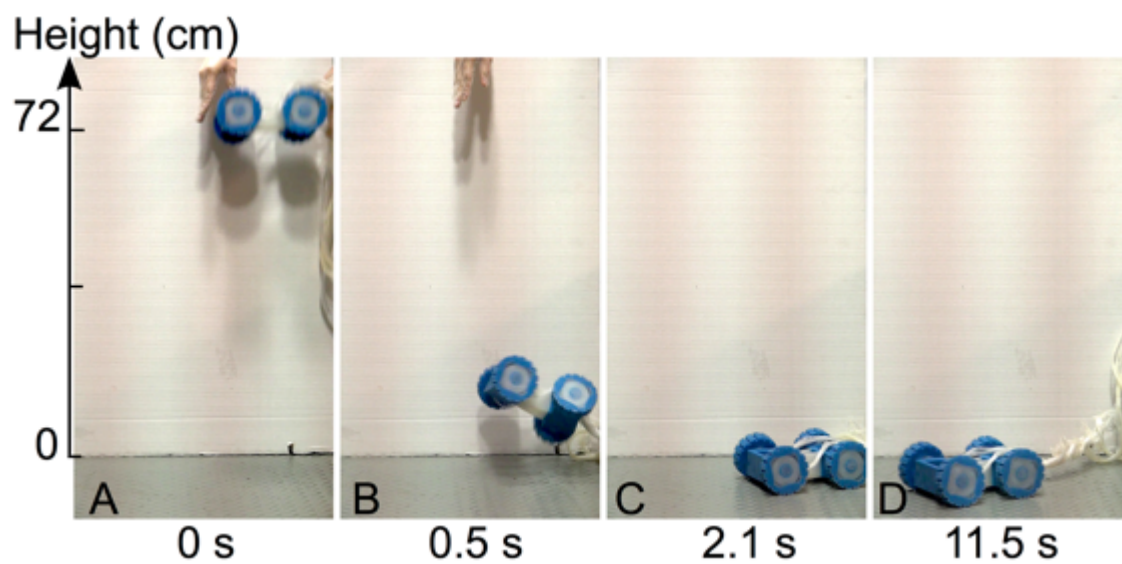
Figure 5. A drop test on a four-wheeled vehicle showing its capability of withstanding mechanical impact. (A) The vehicle is falling from the height of 0.72 m. (B-D) After bouncing once, the vehicle is intact and continues to go forward. (**Movie S5**)
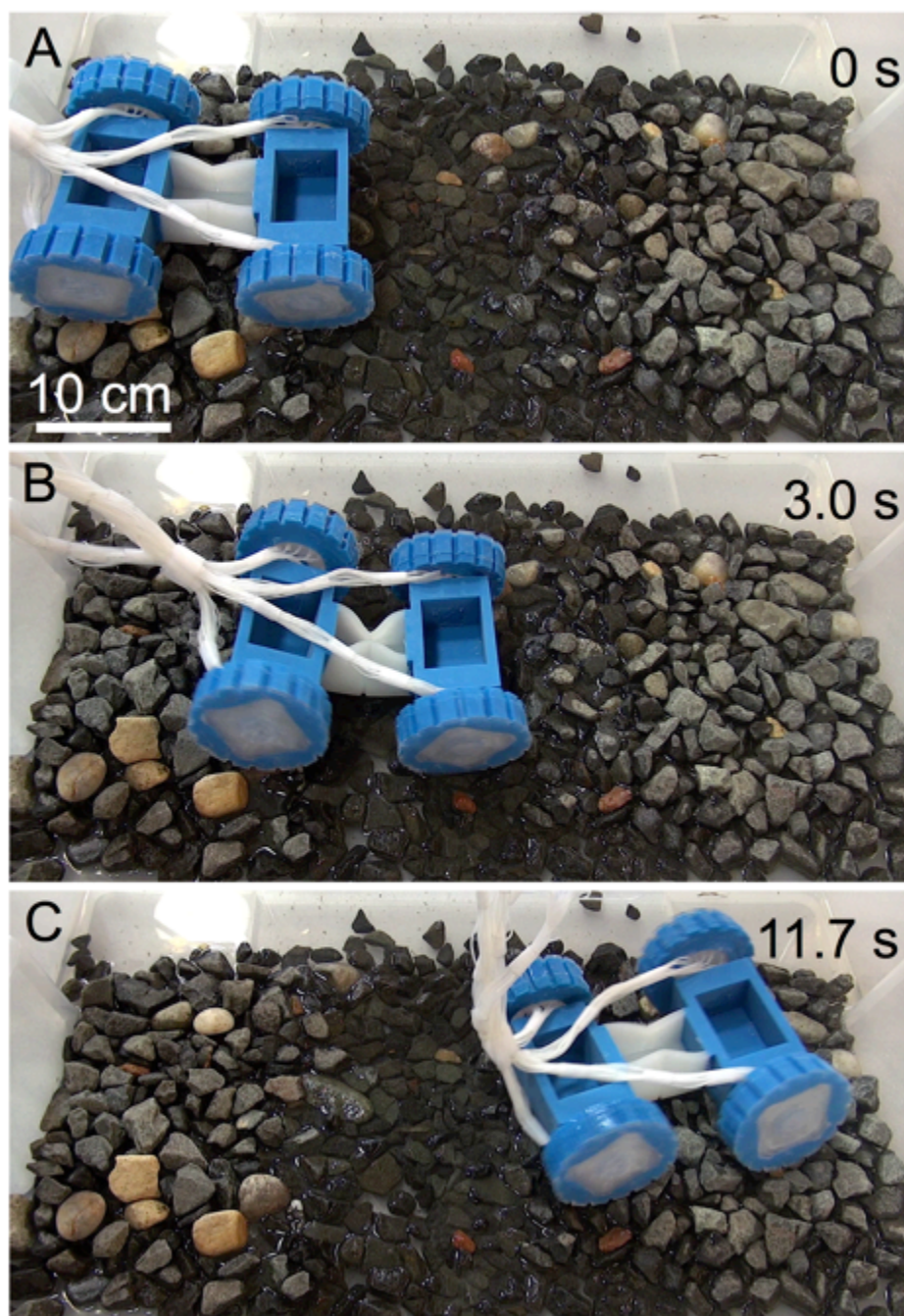
Figure 6. A four-wheeled vehicle negotiating a rocky terrain with a puddle on its way. (A) The vehicle starts at higher level of rocks. (B) The vehicle went down into the puddle with its body bending. (C) The vehicle went up to the other side of rocks. (**Movie S6**)

5. Conclusions

The soft rotary actuators generate motion through biologically-inspired peristalsis that uses alternating inflation and deflation of pneumatic bladders (**Figure 1**). We describe two types of rotary actuators with their complementary configurations of stators and rotors. Type 1 has an internal plastic (ABS) rotor fabricated by a 3-D printer, while Type 2 has an external soft rotor surrounding a stator. Lubricant helps reduce the friction between stators and rotor to achieve a smoother rotation. FEM simulations estimated the local strain of the inflated bladders to ensure the material (Ecoflex 00-50) would not yield or fail. Also the experiments conducted in the same fashion verified the FEM results and implied that there was no delamination on the stators at the pressure ranging from 0 to 55.5kPa (8 psi) (**Figure S2**).

For a given design with specified dimensions (i.e., dimensions of air-filled bladders, wall thickness of the bladders, and the distributions of these bladders on a stator), the speed and torque of the soft actuators depended on at least three factors: pressure/flow rate of the compressed air delivered to the bladders, timing of the solenoid valves, and the load on the actuators. Based on the external load applied to the actuators and a desired rotational speed, we could set the pressure on the regulator and the timing to open/close the valves through a programmable pneumatic system. These rotary actuators have "torque-speed" characteristics similar to those of DC motors (**Figure 3**). The quantitative characterization also serves as an initial baseline to follow for future soft, rotary applications.

A winch equipped with Type 1 actuators combined with a soft gripper in the work demonstrated how different soft robotic systems cooperate and might be capable of more

complex tasks (**Figure S7**). Type 2 actuators enabled the fabrication of a squishy, wheeled vehicle with the ability to withstand mechanical impact (**Figure 5**), negotiate rocky and wet terrains (**Figure 6**), and work under water as an amphibious vehicle (**Figure S9**),

Although the configuration of stator and rotor has solved the issue of the tangled tubing caused by rotational motion, the tubing that supplies pressurized air is still limiting the workspace of the actuators. An onboard, autonomous system for a soft robot is desirable, and still remains a somewhat open challenge[11]. To better understand the soft rotary actuators, we still need to conduct fatigue tests for them and see how the alternating inflation and deflation might change the properties of the material. We can also optimize the design to reduce or avoid stress concentration, and explore alternative elastomers with higher strengths, so that the actuators can possibly have better performance (i.e., longer life and higher rotational speed). In terms of characterization and control, dynamic simulations for the interactions between a stator and a rotor at varied pressures are desirable, to reveal the intrinsic relationship of the inflation and rotation of a rotary actuator.

There is a limitation of the squishy, four-wheeled vehicle: unlike a traditional car, the vehicle has a body with four fixed axles, which requires a different mechanism to make the vehicle turn. Thus, in the demonstrations, we were only focused on the motion in a straight line. To extend the degrees of freedom, we can develop more sophisticated control patterns for each wheel, based on rotational speed and overall dimension of the vehicle. An alternative design, such as a pneumatic, morphing vehicle body, will also potentially inspire more complex motions.

Reference

[1] C.-P. Chou, B. Hannaford, IEEE Trans. Robot. Autom. 1996, 12, 90.

[2] K. Suzumori, S. Iikura, H. Tanaka, in 1991 IEEE Int. Conf. Robot. Autom. 1991 Proc., 1991, pp. 1622–1627 vol.2.

[3] K. Suzumori, S. Endo, T. Kanda, N. Kato, H. Suzuki, in 2007 IEEE Int. Conf. Robot. Autom., 2007, pp. 4975–4980.

[4] F. Ilievski, A. D. Mazzeo, R. F. Shepherd, X. Chen, G. M. Whitesides, Angew. Chem. Int. Ed. 2011, 50, 1890.

[5] R. F. Shepherd, F. Ilievski, W. Choi, S. A. Morin, A. A. Stokes, A. D. Mazzeo, X. Chen, M. Wang, G. M. Whitesides, Proc. Natl. Acad. Sci. U. S. A. 2011, 108, 20400.

[6] S. A. Morin, R. F. Shepherd, S. W. Kwok, A. A. Stokes, A. Nemiroski, G. M. Whitesides, Science 2012, 337, 828.

[7] R. V. Martinez, A. C. Glavan, C. Keplinger, A. I. Oyetibo, G. M. Whitesides, Adv. Funct. Mater. 2014, 24, 3003.

[8] R. V. Martinez, C. R. Fish, X. Chen, G. M. Whitesides, Adv. Funct. Mater. 2012, 22, 1376.

[9] R. F. Shepherd, A. A. Stokes, J. Freake, J. Barber, P. W. Snyder, A. D. Mazzeo, L. Cademartiri, S. A. Morin, G. M. Whitesides, Angew. Chem. 2013, 125, 2964.

[10] B. Mosadegh, P. Polygerinos, C. Keplinger, S. Wennstedt, R. F. Shepherd, U. Gupta, J. Shim, K. Bertoldi, C. J. Walsh, G. M. Whitesides, Adv. Funct. Mater. 2014, 24, 2163.

[11] M. T. Tolley, R. F. Shepherd, B. Mosadegh, K. C. Galloway, M. Wehner, M. Karpelson, R. J. Wood, G. M. Whitesides, Soft Robot. 2014, 1, 213.

[12] N. Correll, Ç. D. Önal, H. Liang, E. Schoenfeld, D. Rus, in Exp. Robot. (Eds.: O. Khatib, V. Kumar, G. Sukhatme), Springer Berlin Heidelberg, 2014, pp. 227–240.

[13] A. D. Marchese, C. D. Onal, D. Rus, in 2011 IEEERSJ Int. Conf. Intell. Robots Syst. IROS, 2011, pp. 756–761.

[14] K. W. Wait, P. J. Jackson, L. S. Smoot, in 2010 IEEE Int. Conf. Robot. Autom. ICRA, 2010, pp. 3757–3762.

[15] E. Brown, N. Rodenberg, J. Amend, A. Mozeika, E. Steltz, M. R. Zakin, H. Lipson, H. M. Jaeger, Proc. Natl. Acad. Sci. U. S. A. 2010, 107, 18809.

[16] L. Margheri, C. Laschi, B. Mazzolai, Bioinspir. Biomim. 2012, 7, 025004.

[17] B. Mazzolai, L. Margheri, M. Cianchetti, P. Dario, C. Laschi, Bioinspir. Biomim. 2012, 7, 025005.

[18] S. Kim, C. Laschi, B. Trimmer, Trends Biotechnol. 2013, 31, 287.

[19] R. V. Martinez, J. L. Branch, C. R. Fish, L. Jin, R. F. Shepherd, R. M. D. Nunes, Z. Suo, G. M. Whitesides, Adv. Mater. 2013, 25, 205.

[20] D. Trivedi, C. D. Rahn, W. M. Kier, I. D. Walker, Appl. Bionics Biomech. 2008, 5, 99.

[21] R. Pfeifer, M. Lungarella, F. Iida, Commun ACM 2012, 55, 76.

[22] F. P. Melo, J. A. Siqueira, B. A. Santos, O. Álvares-da-Silva, G. Ceballos, E. Bernard, Biotropica 2014, 46, 257.

[23] K. Sims, in Proc. 21st Annu. Conf. Comput. Graph. Interact. Tech., ACM, New York, NY, USA, 1994, pp. 15–22.

[24] K. Sims, Artif. Life 1994, 1, 353.

[25] N. Cheney, R. MacCurdy, J. Clune, H. Lipson, in Proc. 15th Annu. Conf. Genet. Evol. Comput., ACM, New York, NY, USA, 2013, pp. 167–174.

[26] W. G. Paterson, GI Motil. Online 2006, DOI 10.1038/gimo13.

[27] S. Maeda, Y. Hara, R. Yoshida, S. Hashimoto, Angew. Chem. 2008, 120, 6792.

[28] M. M. Teymoori, E. Abbaspour-Sani, Sens. Actuators Phys. 2005, 117, 222.

[29] S. Kim, E. Hawkes, K. Cho, M. Joldaz, J. Foleyz, R. Wood, in IEEERSJ Int. Conf. Intell. Robots Syst. 2009 IROS 2009, 2009, pp. 2228–2234.

[30] S. Seok, C. D. Onal, K.-J. Cho, R. J. Wood, D. Rus, S. Kim, IEEEASME Trans. Mechatron. 2013, 18, 1485.

[31] A. N. Gent, Int. J. Non-Linear Mech. 2005, 40, 165.

[32] G. Mao, T. Li, Z. Zou, S. Qu, M. Shi, Int. J. Solids Struct. 2014, 51, 2109.

[33] S. J. Gould, "Kingdoms without wheels," Natural History, vol. 90, no. 3, p. 42,1981.

[34] R. Dawkins, "Why don't animals have wheels?," The Sunday Times, vol. 24, 1996.

Supporting Information

Rotary Actuators Based on Pneumatically-Driven Elastomeric Structures

Supporting Information

Rotary Actuators Based on Pneumatically-Driven Elastomeric Structures

Fabrication of Soft Rotary Actuators

Fabrication of the stators (**Figure S1A**) required the molding and assembly of two separate components: one for the structure with groups of inflatable bladders (top layer) and one for a layer to seal these chambers (bottom layer). We took off the top layer of the stator from the mold at first and then put it on the half-cured bottom layer in the mold after cleaning the surface of the top layer with isopropyl alcohol. Usually it took 10 minutes for the bottom layers to be partially cured at room temperature. After the bottom layer was fully cured, the complete stator was ready to be taken off. The designated dots on the bottom layer indicate the positions of the inlets for compressed air. After punching 16 holes on the bottom layer with needles, we inserted silicone rubber tubing (OD:1/16, ID:1/32) into each bladders through the holes. As the final step, we sealed the gap between the tubing and the holes with silicone rubber adhesive Sil-Poxy (Smooth-On Inc.). In general, the fabrication for the two types of the stators is the same and both of them are made of silicone-based elastomer. However, we have made Type 1 rotors (**Figure S1B**) of a hard, 3-D printed thermoplastic (i.e., ABS), and Type 2 rotor of thermosetting elastomer Mold Star 30 (Smooth-On Inc.).

For Type 2 rotor, 3-D printer produced the molds for the different layers of the external rotor and then we molded these layers (**Figure S1C**). We bonded the layers with Sil-Poxy. There are three layers: one layer with the main structure designed to interact with the stator inside of it, one PDMS layer to constrain the slide on the axial direction between

the rotor and the stator, and one layer that constrains and fixes the stator on the other side. The transparency of the PDMS layer also shows the internal structures and helps us monitor how the rotor and the stator interact when controlling an actuator. The material for the other two layers (blue) is Mold Star 30 (Smooth-On Inc.). Mold Star 30 is a type of platinum silicone rubber, which is also an elastomer, but it is stiffer than the Ecoflex series.
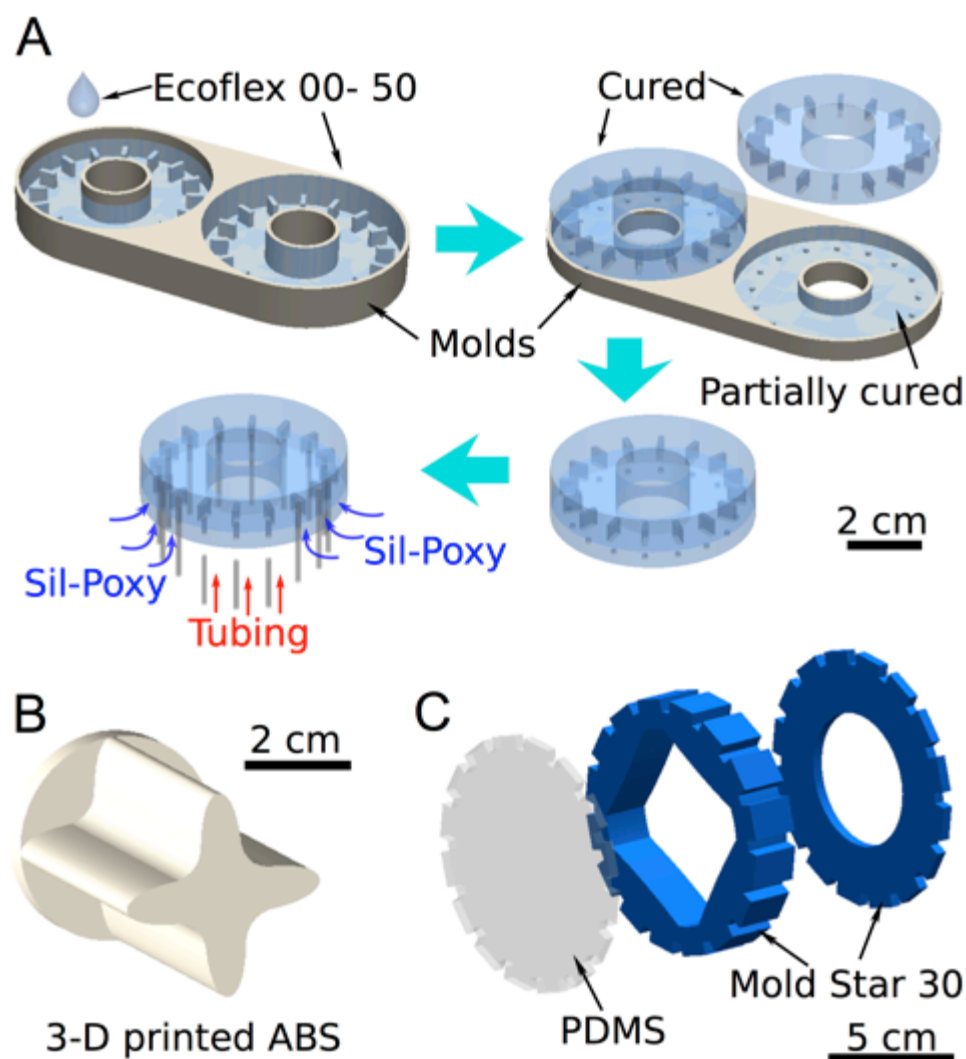
Figure S1. Meso-scale soft lithography of the rotary actuators. (A) A 3-D printed mold patterns cast Ecoflex into the thick portion of a stator. After curing the thick portion of the stator, it bonds to a thin cover of Ecoflex that is partially cured and adhesive. The tubing then goes into the molded bladders of the stator with Sil-Poxy providing an adhesive sealing. (B) A rotor of Type 1, which was fabricated with ABS by a 3-D printer. (C) A rotor of Type II consists of three layers, which surrounded an internal stator (not pictured).

Simulated and Experimental Behavior of Inflation with Static Internal Pressures

To explore how a static internal pressure acted on the bladders of a stator and whether the pressure made the material fail, we performed FEM simulations based a 3rd-ordered Yeoh model of Ecoflex 50-00 (**Figure S3**). According to the simulated results presented in **Figure 2SB, D**, the maximum principal strains did not exceed 2 for both types of stators if the internal pressure of the bladders was less than 62.1 kPa (9 psi). The simulations revealed that the maximum principal strain experienced by the bladders of the stator was lower than 980% – the maximum strain at break of Ecoflex 50. [According to the manufacturer's data sheet]

In addition, the experimentally acquired images of the stators with one subgroup of bladders inflated (**Figure S2 A, C**) suggested that the simulated results were similar to the experiments at the same pressures. Thus, the FEM simulation was valid and acceptable. According to **Figure S2 A, C**, increasing the static internal pressure enlarged the deformation of the bladders. With 41.4 kPa (6 psi) of applied pressure, the deformation was not conspicuous. An abrupt change in volume (i.e., passing through snap-through instability)[31,32] occurred when the measured internal pressure went from 48.3 kPa (7 psi) to 55.2 kPa (8 psi). The sudden large deformation of the imbedded bladders would force the rotor to turn. We also hypothesize that the rapid expansions with their sudden releases of kinetic energy may also facilitate the forcing of the actuator through its metastable states. Furthermore, the experiments also revealed that the increasingly enlarged deformation of the inflated bladders (after passing through the

snap-through instability) did not show any delamination between the two layers of the stator, which proved the feasibility of the design, and validated the methods of fabrication.
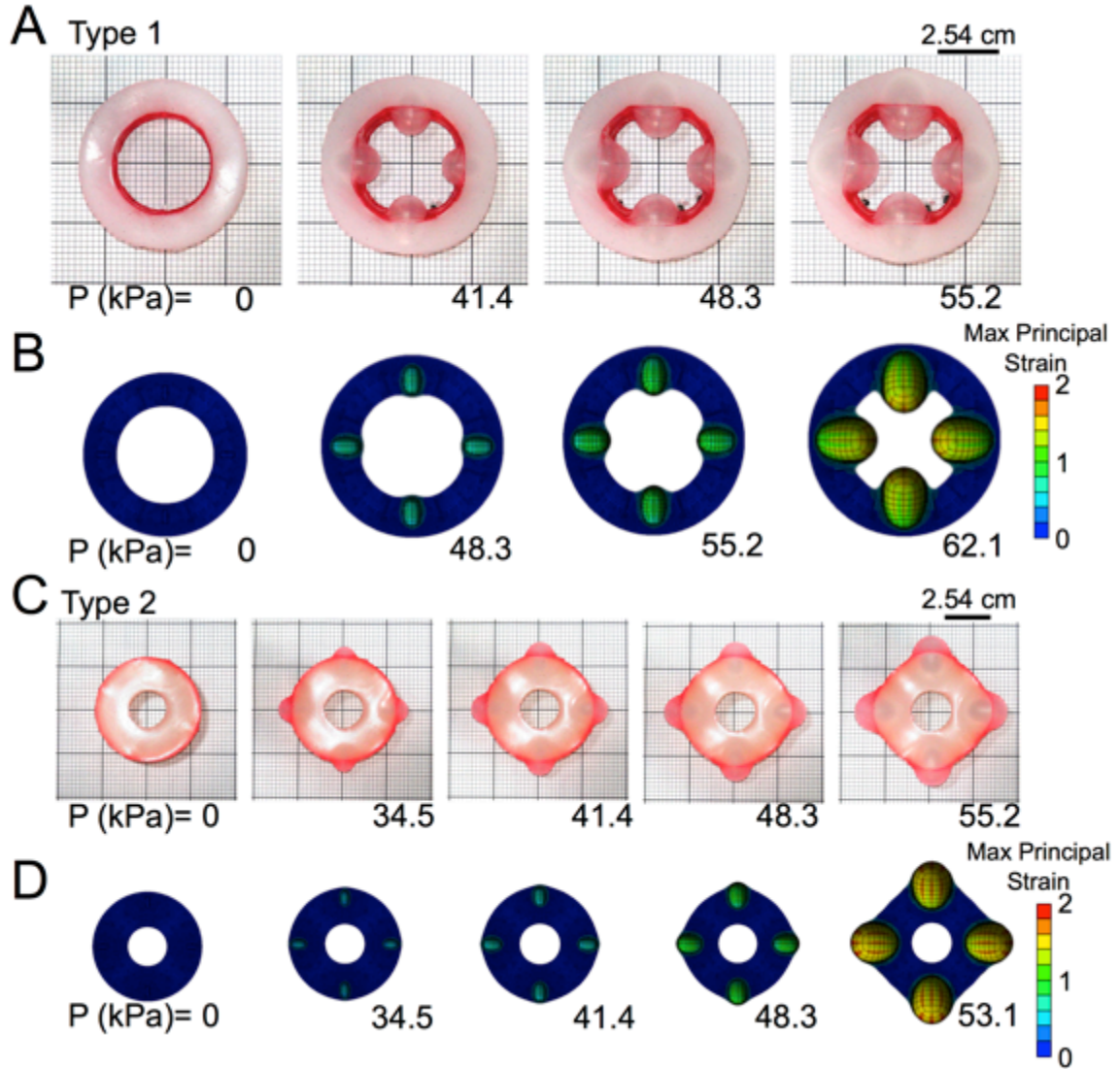
Figure S2. (A, C) Experimental tests on the behavior of two types of stator with static internal pressure up to 55 kPa (8 psi). (B, D) Simulated behavior of the stators showing the deformation and maximum principal strain as a function of internal pressure up to 53 kPa (7.7 psi). We hid the tubing that provided pressurized air behind the meshed background.

Uniaxial tensile tests of Ecoflex 00-50 and Yeoh model

To look into the relationship between the static internal pressure and the deformation of the bladders on a stator, and whether the corresponding principal strain would exceed the breaking point of the elastomeric materials (Ecoflex 00-50), we performed finite-element simulations of the inflations in ANSYS by importing the designed geometry of the stators. **Figure S3** shows the engineering stress-strain curves of Ecoflex 00-50 from tensile data of five degassed and cured samples. The green curve is plotted with the mean values of the five samples, and the blue curve is the stress-strain curve of one of these five samples. We considered the material as a hyper-elastic solid and fitted the test data to the Yeoh hyper-elastic material model with the module for curve fitting in ANSYS Workbenck, and then plotted the curves in MATLAB (shown as red curves), which has been adopted by Mosadegh, et al.[10]The strain energy density of nearly-incompressible Yeoh model (that was also shown by Mosadegh, et al.[10]) is described as

$$U = \sum_{i=1}^{N} C_{i0} \left(\overline{I}_1 - 3 \right)^i + \sum_{i=1}^{N} \frac{1}{D_i} \left(J - 1 \right)^{2i} \tag{2}$$

where $\overline{I}_1 = tr \left[dev \left(\mathbf{FF} \right)^T \right]$, $J = \det \left(\mathbf{F} \right)$, and $\mathbf{F}$ is the deformation gradient and C_{i0} and D_i are the materials parameters. When we set N = 3 (3rd-ordered Yeoh model), the curve fitting module in ANSYS calculated the parameters. For the mean data of the five samples, we have $C_{10} = 1.90 \times 10^{-2}$, $C_{20} = 9.0 \times 10^{-4}$, $C_{30} = -4.75 \times 10^{-6}$, $D_1 = D_2 = D_3 = 0$. For the data of the sample, the parameters are $C_{10} = 1.75 \times 10^{-2}$, $C_{20} = 6.70 \times 10^{-4}$, $C_{30} = -2.65 \times 10^{-6}$, $D_1 = D_2 = D_3 = 0$.

In this paper, we chose the sample data to perform the static simulations. By varying the applied pressure inside of embedded bladders, we got the deformation of the bladders and the estimated principal strain shown in **Figure S1B, D**. According to results of the simulations, the maximum principal strain of the inflated bladders was 2, which means the region of most interest on the curve is the strain of 0-200% indicated in **Figure S3** (Bottom).
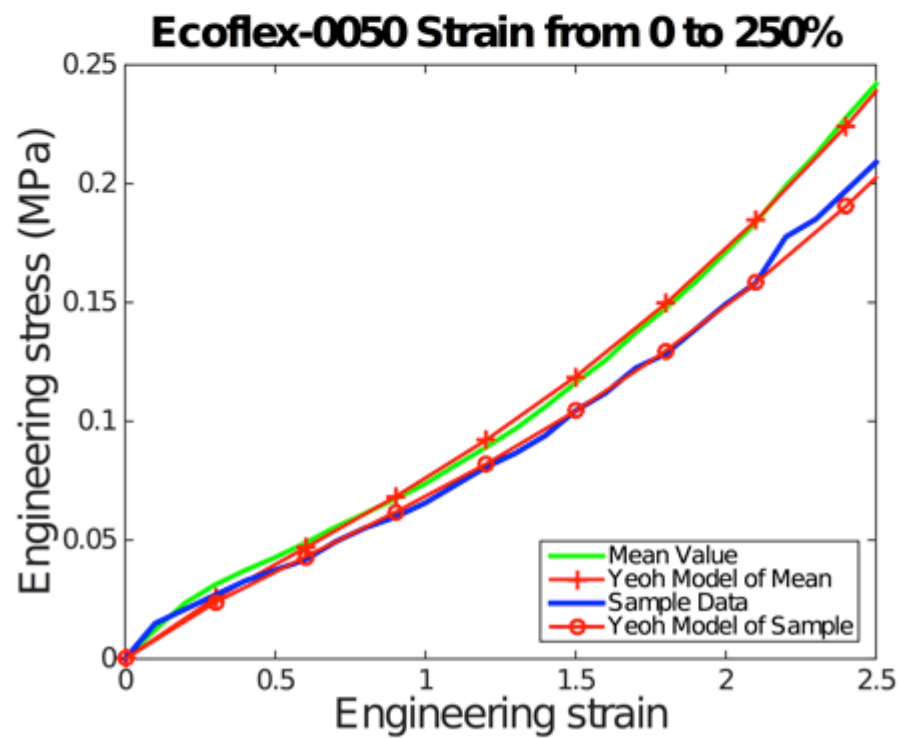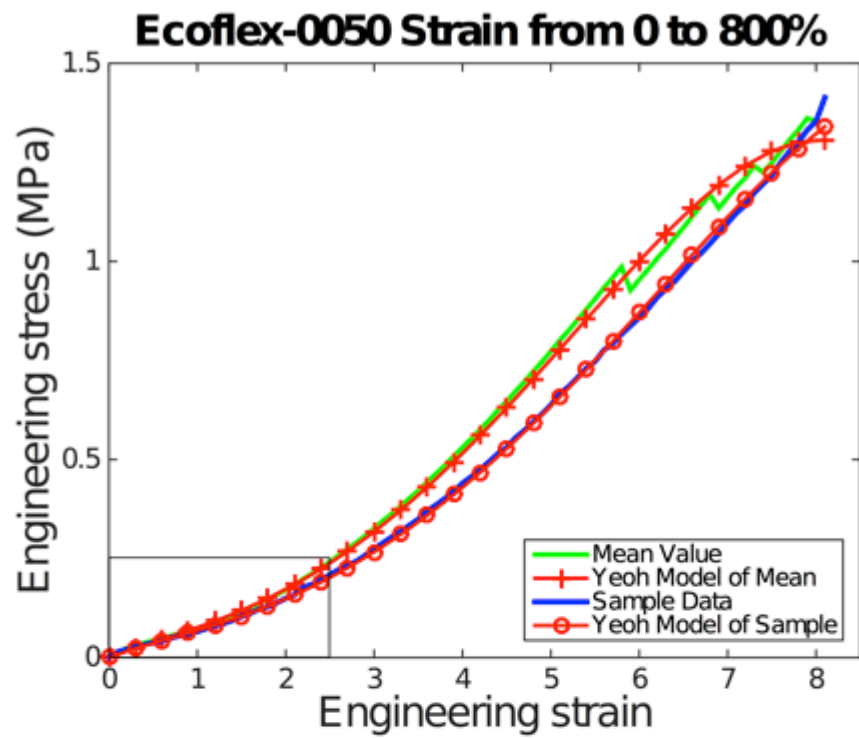
Ecoflex-0050 Strain from 0 to 800%

Ecoflex-0050 Strain from 0 to 250%

Figure S3. Stress-strain curve and Yeoh model of Ecoflex 00-50. Top: Uniaxial tensile test (blue solid line) of the elastomer (Ecoflex 00-50) used for simulations of the stators inflated by varied static pressures. We fitted the stress-stain curve with Yeoh model of hyperelasticity (red dotted line). Bottom: The region of most interest (strain: 0 to 250%) since the principal strains were less than 2, according to the simulations.

Programmable Pneumatic System

Two NI 9474 modules provided 16 digital outputs to drive 16 directional control valves (SMC Inc.). **Figure S3** is a schematic of the system. This system allows us not only to control manually each valve through the keyboard but also to import a spreadsheet with the information of the control pattern (timing and a specific sequence) of the actuation of the valves and achieve the automatic control.

The use of NI cRIO-9076 module allowed high speed and high accuracy of timing. NI 9474 can reach 1 μsec high-speed digital output, which allows us to precisely control on/off of the valves with fast response.
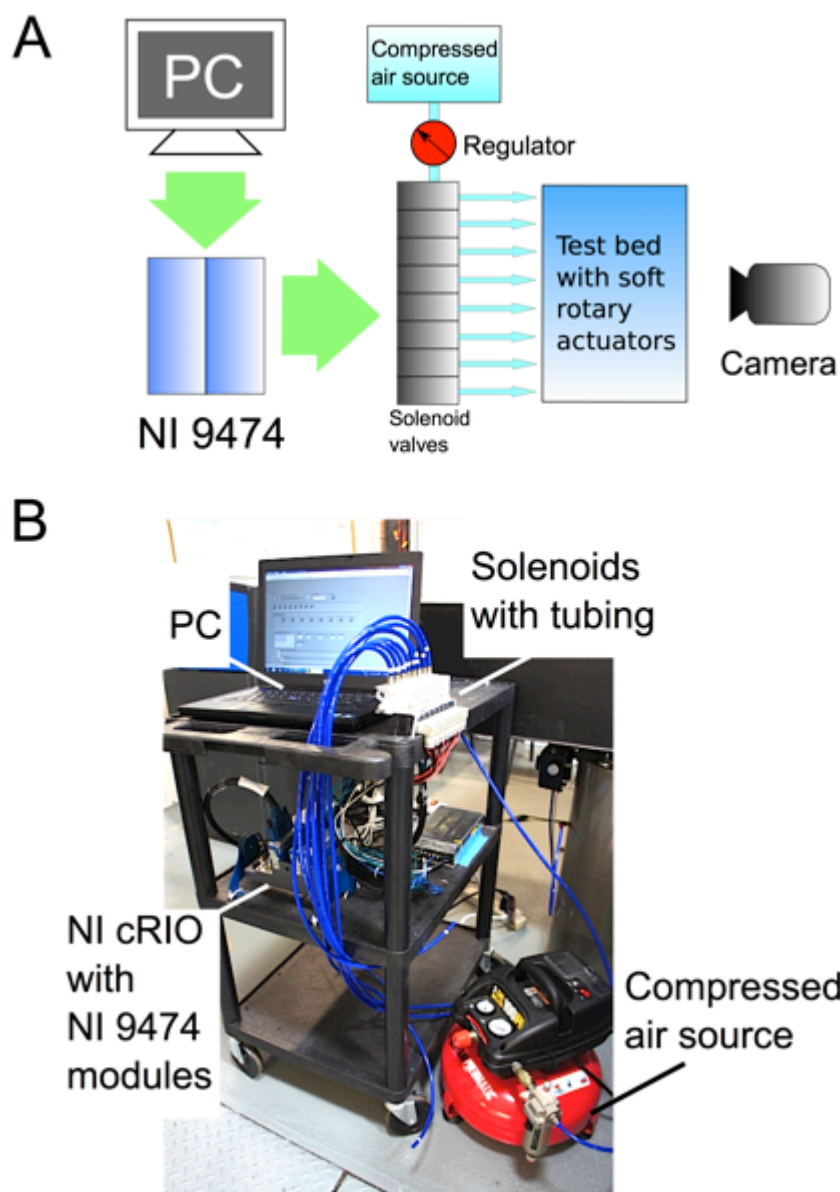
Figure S4. Pneumatic System. (A) Schematic of the programmable pneumatic system used for soft rotary actuators. (B) A photo of the setup carried on a cart. (The pressure regulator and the camera are not shown in the photo.)

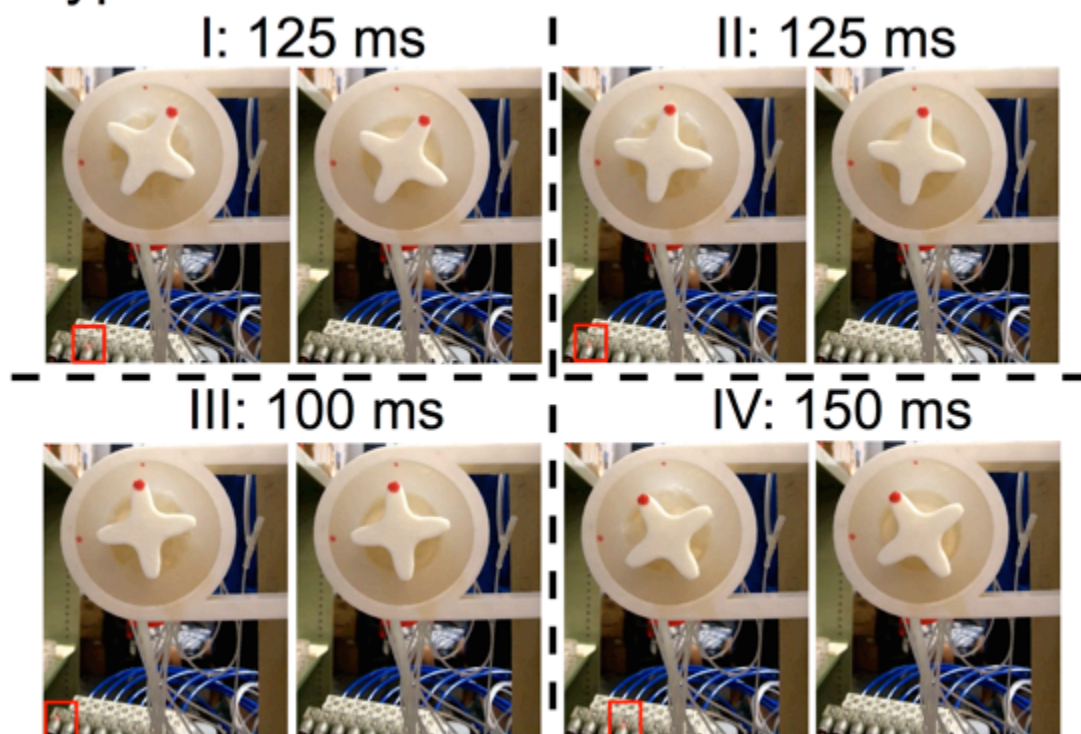*Estimating Deflation Times with High-Speed Camera*

As discussed in the paper, increasing pressure leads to a higher rotational speed due to an increased inflation time $t_{inflation}$ (**Equation 1**). However, the deflation times remain relatively consistent for a given volume of the inflated bladders. To estimate the rotational speed of a rotary actuator, we found the deflation times for both types of actuators using a high-speed camera (**Figure S5**, **Movie S1**).

Instead of sending command signals (**Figure 2A**) to the valves, we manually open a valve for one subgroup of bladders with a keyboard. Starting from a very low pressure, we gradually increased the pressure with the regulator, until the inflation of these bladders just reached the minimum that could enable a rotation from this subgroup to an adjacent subgroup. The volumes would not grow even if we kept the valve open. Thus, the pressure on the regulator (~ 48.4 kPa, 7 psi) reflected the static internal pressure of these inflated bladders. And then, we closed the valve to exhaust the bladders. By observing and counting the frames (acquired from high-speed videos) between closing a valve (indicated by the LED lights on the valves) and a complete exhaustion of a group of bladders, we were able to calculate a deflation time for this group. We did nine groups of experiments for Type 1 and four groups of experiments for Type 2.

Figure S5 summarizes four groups of experiments for each type of actuator. For each group, we picked the frame showing the LED light on a valve was about to go out, and the frame showing the shape of the stator was completely restored. The speed of the camera we used was 120 frames/sec. By counting the number of total frames between two frames we picked, we were able to calculate the period in between, which is the

deflation time $t_{\text{deflation}}$. We indicated the calculated $t_{\text{deflation}}$ for each experiment in the

figure. The average $t_{\text{deflation}}$ for Type 1 is 125 msec (130 msec if using nine experiments),

and the average $t_{\text{deflation}}$ for Type 2 is 190 msec.

A Type 1

I: 125 ms   II: 125 ms

III: 100 ms   IV: 150 ms

B Type 2

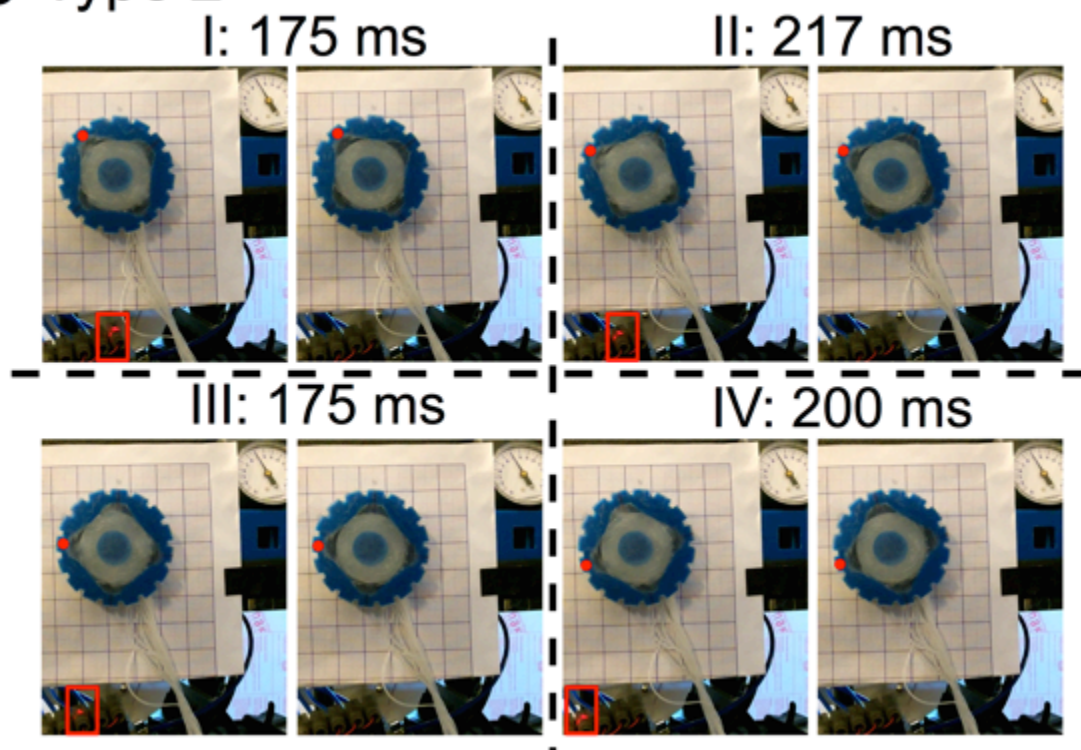I: 175 ms   II: 217 ms

III: 175 ms   IV: 200 ms

Figure S5. Estimation of deflation times using high-speed videos. (A) Four groups of deflation of a Type 1 stator suggested an average deflation time $t_{\text{deflation}} = 125\,\text{msec}$. (B) Four groups of deflation of a Type 2 stator gave an average deflation time $t_{\text{deflation}} = 190$ msec. The red boxes indicate the LED light that would go out in the next frame.

Prototyping the winch for Type 1 Actuators

In order to characterize "torque-speed" curve for Type 1 actuator easily, we designed and prototyped a winch equipped with Type 1 actuators (**Figure S6)**. A 3-D printed cylindrical shaft couples two Type 1 rotors through the cross-shaped hole. A string attached to the shaft carries external loads for characterization. (**Figure S6 A**) Two 3-D printed brackets hold the insides of two stators and the tubing on the stators can easily pass though the 16 small inlets on each bracket. (**Figure S6 B**) A stand made of wooden boards attached with the brackets form the whole frame of the winch. After equipping the stators in the brackets and inserting the shaft into the stators, we were able to profile the "torque-speed" relationship for Type 1 actuator, by varying the load added onto the winch. (**Figure 3C**)
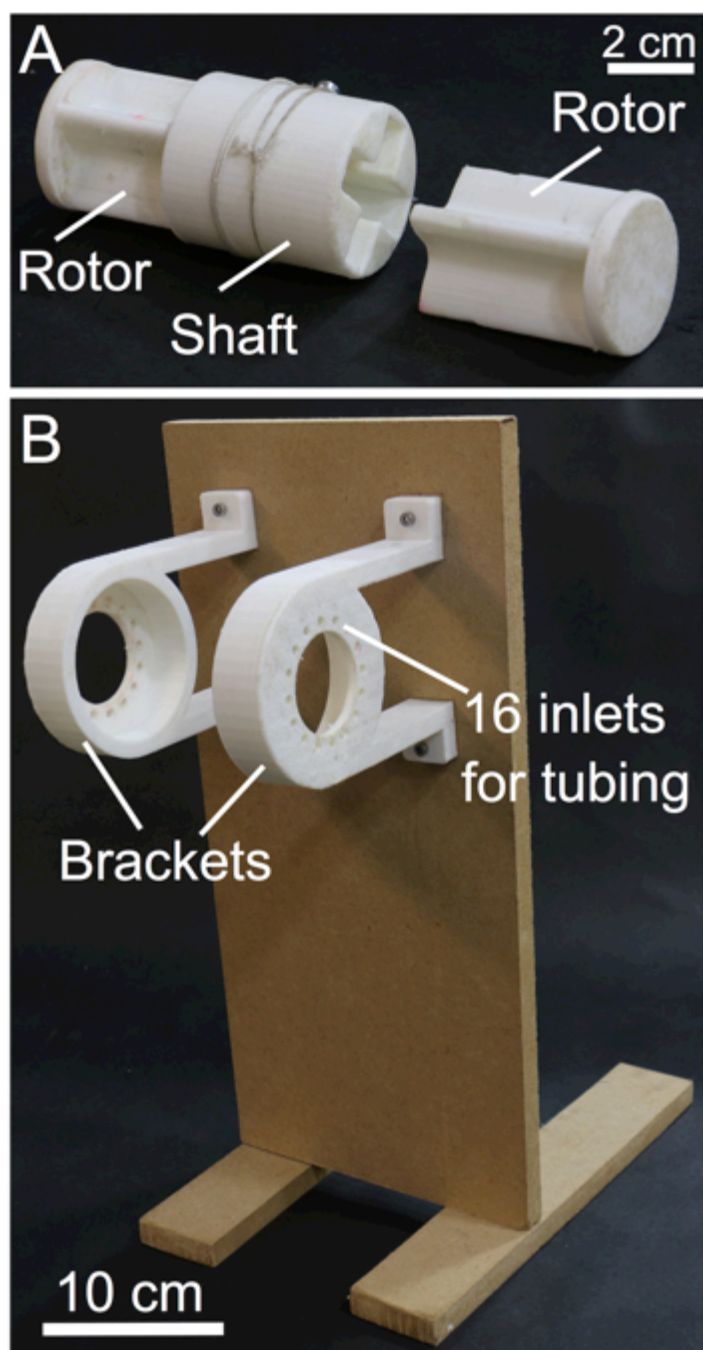
Figure S6. A prototype of the winch designed for Type 1 actuators. (A) A 3-D printed cylindrical shaft coupled with two Type 1 rotors. (B) Two 3-D printed brackets fixed on a wooden stand.

A Winch with a Soft Gripper

We attached a soft gripper (16.4 grams) with embedded PneuNets[4] on the winch, showing that we can combine soft rotary actuators with different kinds of soft actuators to build multi-functional soft systems. The previous section in Supporting Information discussed the design of the winch (**Figure S6**). With a 3-D printer printing the molds, we fabricated a soft robotic gripper from Ecoflex 00-30 (Smooth-On Inc.) for the extensible layer, and Mold Star 15 (Smooth-On Inc.) for the inextensible layer. Silicone tubing (independent of the pneumatic system) supplied the compressed air to the gripper through a manually controlled syringe.

Figure S7 and **Movie S2** demonstrates how this winch picked up and lifted an object (30.7 grams) with the imported control sequence ($t_{\text{inflation}} = 370$ msec and $t_{de\text{flation}} = 130$ msec) of the pneumatic system. The winch would work at a rotational speed of 7.5 RPM. Based on the characterization of Type 1 (**Figure 3C**) at a set pressure of 68.9 kPa (10 psi), the minimum speed is around 13.8 RPM. Therefore, we needed to lower the set pressure to achieve a lower rotational speed (7.5 RPM) used for this demonstration. Here, we used a set pressure of approximately 55.1 kPa (8 psi).

The external torque on the winch was 3.2×10^{-3} Nm, which was estimated with the mass of the gripper. Thus, the torque acting on each stator was 1.6×10^{-3} Nm. Starting at the top (Height $\cong 22$ cm), the winch lowered the gripper at a rate of 1.7 cm/sec (**Figure S7 A-B**). After the shaft turned in 11 steps, the gripper reached at the position (Height $\cong 13$ cm) shown in **Figure S7 B**. When the gripper contacted the object at Height = 0, we actuated the gripper to grasp the object, by compressing the air into the embedded

PneuNets through a syringe. Then, the winch started lifting the gripped with the object. The external torque on the winch increased to 9.2×10^{-3} Nm due to the mass of the object. In order for the winch to carry heavier load at the same speed, we slightly increased the pressure on the regulator. In **Figure S7 C-D** (Height: from 0 to 14 cm), the winch raised the gripper and the object at a rate of 1.6 cm/sec, turning in around 17 steps.
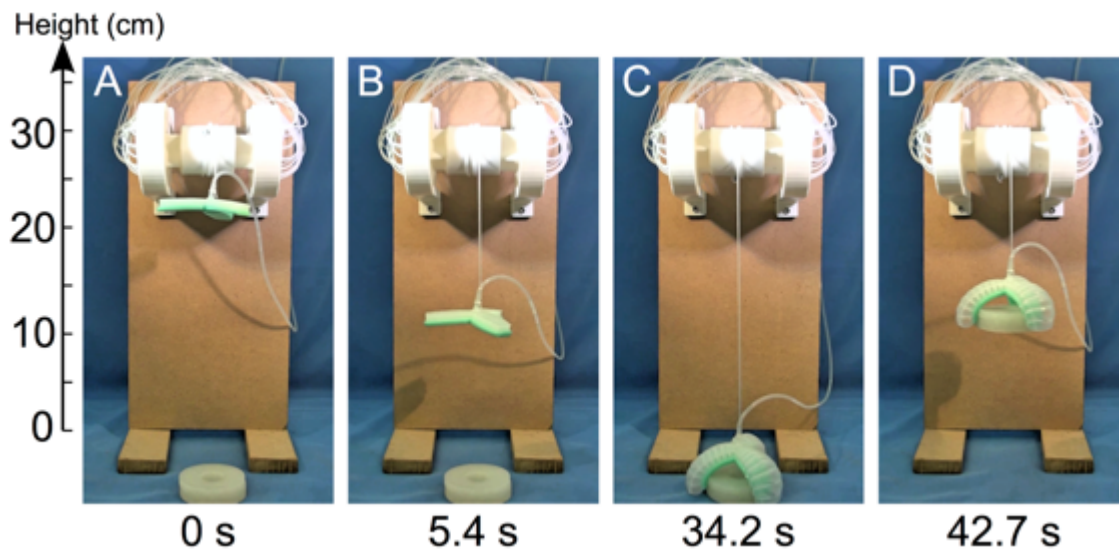
Figure S7. A winch equipped with two Type 1 stators acting in parallel and a soft gripper (16.4 grams) that could grasp and lift an object weighted 30.7 grams. (A) The gripper started at the top. (B) The winch lowered the gripper at a speed of 1.6 cm/sec. (11 steps of the rotor). (C) The gripper inflated and grasped the object. (D) The winch raised the gripper and grasped object at a rate of 1.6 cm/sec (17 steps of the rotor).

A Squishy, Two-Wheeled Vehicle

The basic design consisted of an elastomeric body and two axles made of Mold Star 30 (Smooth-On Inc.), and two Type 2 actuators (**Figure S8 A**). In case the parallel-wheeled device would lose its balance (like a monocycle) and not be able to function as a real vehicle, we attached a paperclip to each end of the body as supports (**Figure S8 B**). Directed by the designed command pattern for each wheel, the two-wheeled vehicle demonstrated its ability to navigate around an obstacle (**Figure S8 C-H**) (**Movie S3**). This vehicle presented the capability of going forward, going backward, and turning. The input pressure was 86.2 kPa (12.5 psi) and the corresponding inflation time was around 180 msec. Based on **Equation 1**, the rotational speed was 10.25 RPM. Considering the diameter of the wheels was 9.2 cm, the speed of the two-wheeled vehicle was 4.9 cm/s.
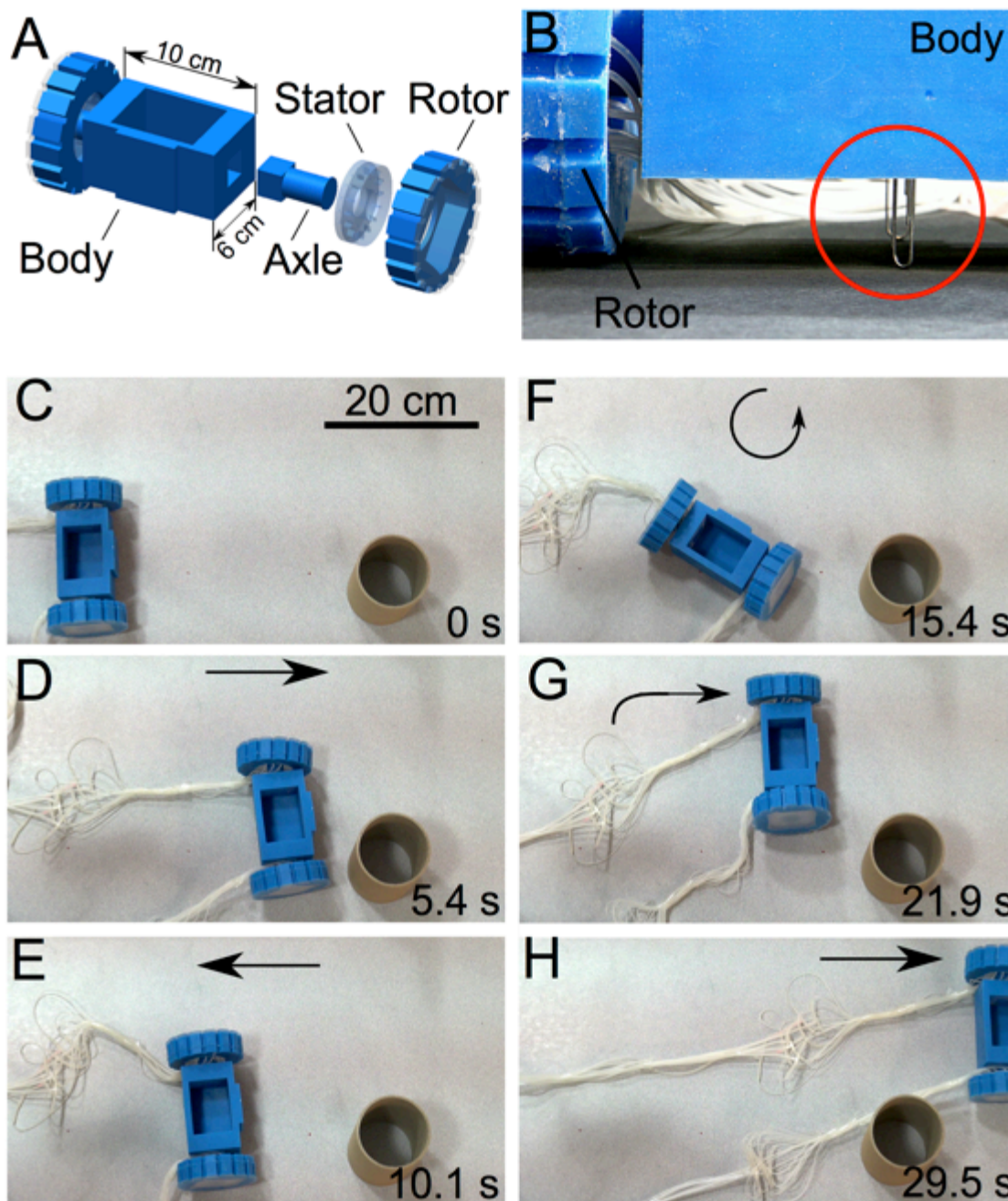
Figure S8. (A) Design of the squishy two-wheeled vehicle, (B) The highlighted pieces are two paperclips used to balance the vehicle. (C-H) To navigate around an obstacle on its way, the two-wheeled soft vehicle moved forward, stopped, moved backward, made a left turn, went forward, turned back to straight and then went forward. The arrows indicate the moving directions of the vehicle.

A Squishy, Four-Wheeled Vehicle Working Under Water

Lacking any electronic components or metal members, the prototype of a four-wheeled vehicle was able to work under water (**Figure S9**). To compensate for the buoyancy of water and enhance the traction between the elastomeric wheels (Type 2 rotors) and the water tank, we loaded rocks on the body of the vehicle. At the pressure of 86.2 kPa (12.5 psi) set on the regulator, the vehicle traveled around 37 cm under water at the speed of 3.6 cm/sec. The demonstration might potentially provide possibilities of low-cost amphibious vehicles.
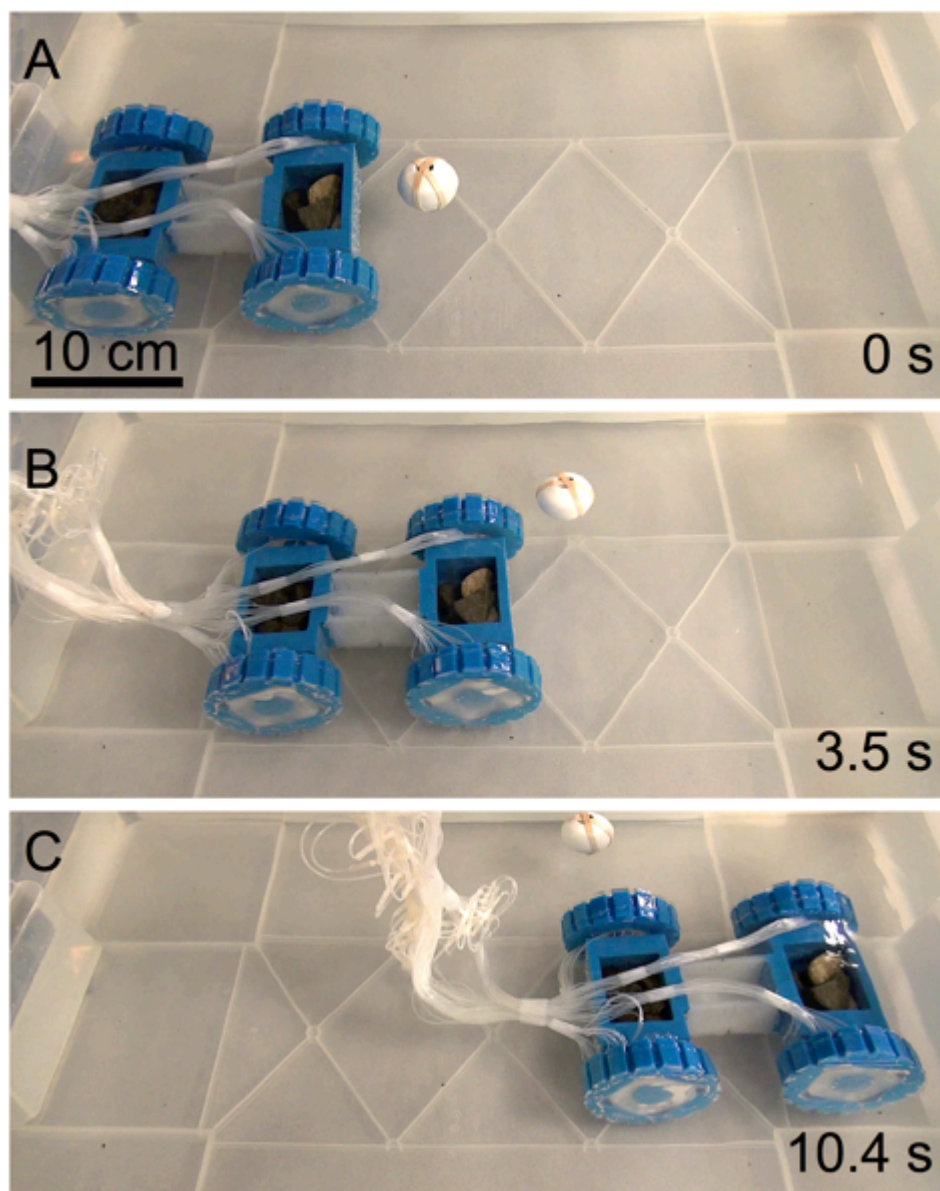
Figure S9. A squishy, four-wheeled vehicle carried rocks and moved forward under water at a speed of 3.6 cm/sec, driven by the pneumatic system. A floating plastic ball indicated the level of the water in tank.